JOURNAL OF MECHANICAL ENGINEERING AND SCIENCES (JMES)
ISSN: 2289-4659 e-ISSN: 2231-8380
VOL. 14, ISSUE 4, 7328 – 7347
DOI: https://doi.org/10.15282/jmes.14.4.2020.02.0576

ORIGINAL ARTICLE

Numerical analysis on the use of multi-element blades in a horizontal-axis hydrokinetic turbine

J. Aguilar[1], L. Velásquez[1*], A. Rubio-Clemente [1-2] , and E. Chica[1]

[1] Departamento de Ingeniería Mecánica, Facultad de Ingeniería, Universidad de Antioquia UdeA, Calle 70, No. 52-21, Medellín, Colombia
Phone: +5742198553; Fax: +5742638282
[2] Facultad de Ingeniería, Tecnológico de Antioquia–Institución Universitaria TdeA, Calle 78b, No. 72A-220, Medellín, Colombia

ABSTRACT – The blades of a hydrokinetic turbine have a great impact on its performance due to they are the elements responsible for capturing the kinetic energy from water and transform it into rotational mechanical energy. In this work, numerical analyses on the performance of a multi-element blade section were developed. The lift and drag coefficients (C_L and C_D, *respectively*) of the hydrofoils with traditional and multi-element configurations were studied. For this purpose, 2D numerical analyses were conducted by using JavaFoil code. S805, S822, Eppler 420, Eppler 421, Eppler 422, Eppler 423, Eppler 857, Wortmann FX 74-CL5-140, Wortmann FX 74-CL5-140 MOD, Douglas/Liebeck LA203A, Selig S1210, Selig S1223 and UI-1720 profiles were tested. The results indicated that the Eppler 420 multi-element hydrofoil provided high efficiency to the turbine. This was attributed to its higher relationship between the maximum C_L and C_D (C_{Lmax}/C_D), which was equal to 47.77, compared to that of the Selig S1223 profile (39.59) and other hydrofoils studied. Therefore, the final optimized blade section selected was an Eppler 420 multi-element hydrofoil with a flap chord length of 70% of that of the main profile. The hydrodynamic and structural designs of the optimized blade section were validated with detailed 3D numerical models, through ANSYs Fluent software. The fluid and structural domains were connected using one-way coupling. The influence of the blade geometry and the operational parameters on the stresses supported by the blades were found by analyzing the fluid-structure interaction. From the numerical analyses conducted, it was observed that the blades did not exhibit structural fails. In this regard, the multi-element hydrofoil might be used for the design of a horizontal-axis hydrokinetic turbine with a high efficiency.

ARTICLE HISTORY
Received: 07th Sept 2019
Revised: 05th May 2020
Accepted: 11th May 2020

KEYWORDS
Multi-element blade;
hydrokinetic turbine;
hydrodynamic analysis;
chord length;
JavaFoil code;
CFD;
Gurney flap

INTRODUCTION

Harnessing the kinetic energy from rivers is regarded as an attractive option to produce electricity in regions of developing countries with geographical difficulties for extending the electricity transmission line [1]. Regardless of the governmental efforts and actions of non-governmental institutions to extend electricity to these isolated areas, the progress in this direction is marginal and extremely slow [2]. In this way, among the different renewable energy technologies, the power generation through the application of hydrokinetic turbines seems to be the most appropriate solution for providing energy at large and small scales in remote areas containing a vast number of rivers [2, 3].

The power generation using hydrokinetic turbines is not associated with the negative environmental impacts generated by large hydroelectric plants [4, 5]. In addition, dams are not required to store energy. Furthermore, hydrokinetic turbine installations do not interfere with the natural course of the rivers and the flood of large forest areas is not needed, which prevents the local displacements of native people, as well as the extermination of natural life in the area [6-9].

The design of hydrokinetic turbines is simple and are easy to be installed in free-flowing rivers or streams for the energy extraction improvement. Additionally, local population inhabiting rural and remote areas can be in charge of hydrokinetic turbine maintenance at a low cost. These aspects make the hydrokinetic turbines a highly competitive technology for producing energy in comparison with conventional hydropower plants [1, 2] and other power supply options, such as stand-alone photovoltaic systems, small hydropowers, wind turbines, diesel generators and grid extension lines [2].

In the hydrokinetic turbine configuration, the blade is the main component [2]. The role of a blade in this kind of turbines is to obtain the energy from water and transform it into rotational mechanical energy. In general, the performance, efficiency and stability of the turbine are greatly influenced by the geometry of the blade and the shape of the hydrofoil used. The blades of a turbine are utilized to generate a lift force for rotating and, subsequently, extracting the optimum power from the system [1, 2]. The design process of a blade mainly includes its hydrodynamic and structural designs in order to obtain its optimal configuration [10, 11].

An optimal blade design can be obtained using flaps or slats in a multi-element hydrofoil configuration due to these geometric configurations can increase the lift to drag ratio (L/D), the lift coefficient (C_L) and the structural efficiency [12, 13]. It is important to note that L/D can be found by dividing C_L over the drag coefficient (C_D); i.e., C_L/C_D. This

*CORRESPONDING AUTHOR | L. Velásquez | ✉ lisabel.velasquez@udea.edu.co

configuration is already used in the racing car industry to improve the ground adhesion of the car at very high speeds. It is also used for aircraft application to achieve a high C_L and increase the stall angle of attack (α) [14]. For example, numerical studies carried out by Smith showed that multi-element airfoil systems have complex flow characteristics as numerous effects govern the flow around these systems [13]. Therefore, the complex flow characterization around the multi-element airfoil is required during the wing design.

It is important to note that in the field of hydrokinetic and wind turbines, few studies on the use of multi-element hydrofoils or airfoils are reported [12, 15]. As a matter of fact, Raghed and Selig employed the multi-element airfoil configuration for a horizontal-axis wind turbine [12] in order to reduce the drag generated by the large root sections without compromising the blade strucural integrity. Seven multi-element airfoil configurations with several combinations of flaps, slats and struts were analyzed. These configurations demostrated the capability to produce significantly higher C_L/C_D and C_L than the traditional DU 00-W-401 airfoil, obtaining a C_L/C_D increase of up to 82%. On the other hand, Narsipur et al. conducted a 2D numerical simulation to study five configurations of the multi-element airfoil system varying the flap deflection, the gap and the overhang in order to understand the effect of these geometric parameters on the system performance [16]. The geometric confinguration consisted of a main element and two flap elements. The results informed that changes in these parameters between each element can increase the aerodynamic efficiency of the multi-element airfoil system. However, the authors concluded that the optimal location of the flaps cannot be defined due to the complex coupling of the effects associated with the parameter variation [16]. In turn, Yavez et al. studied a hydrofoil–slat arrangement for hydrokinetic and wind turbine applications. The authors found that the C_{Lmax} generated increased from 1.45 to 2.78 in comparison with the traditional geometric configuration. The numerical results showed a maximum power coefficient (C_{pmax}) of 0.506. They concluded that the slat-hydrofoil or airfoil arrangements may be applied in the design of wind and hydrokinetic turbines [17]. Recently, Aguilar and coworkers designed and optimized a multi-element hydrofoil for a horizontal-axis hydrokinetic turbine employing a hydrofoil-flap arrangement [18]. For this purpose, 2D Computational Fluid Dynamics (CFD) simulations and multi-objective optimization methodology based on surrogate modelling were used. The Eppler 420 hydrofoil was utilized for the design of the multi-element hydrofoil. The multi-element design selected as the optimal one had a gap of 2.825% of the chord length (C_1), an overlap of 8.52 %C_1, a flap deflection angle (δ) of 19.765˚, a flap chord length (C_2) of 42.471 %C_1 and a α of –4˚. In spite of these studies, further researches related to the impact of multi-element hydrofoil configurations and the values of geometric parameters defining the configuration on the performance of the blade are required. Nevertheless, it must be highlighted that the multi-element configuration increases the overall complexity of the blade design and may present challenges during the manufacturing process for the complex geometry and structures associated with the flap and slat support.

On the other hand, there are other devices used to enhance the lift, such as the Gurney flap, which consists of a small plate located perpendicularly to the trailing edge of the airfoils on their pressure side. Liebeck was the first one reporting an increase in the aerodynamic performance by the use of Gurney flaps in aircraft applications [19]. The results of this study showed that an increase in the region of attached flow in the upper side of the airfoil with a recirculation region behind the Gurney flap led to a rise in the lift with low drag penalty. However, according to the authors' knowledge, the influence of the Gurney flap on the geometric configuration of a multi-element blade for horizontal-axis hydrokinetic turbines has not been investigated yet, since the studies reported in the literature on the field have been focused on wind turbines with traditional hydrofoils [20, 21].

Under this scenario, with the purpose of designing a high-performance rotor of a horizontal-axis hydrokinetic turbine of 1 kW, a detailed CFD study was performed using ANSYs Fluent software and JavaFoil code for examining the influence of a multi-element blade on the turbine efficiency. The analyses were conducted on several airfoils, which were used as hydrofoils, with a traditional and a multi-element flap configuration, including a Gurney flap. The blade section of the hydrokinetic turbines was selected based on C_L and C_L/C_D values, aiming at their maximization.

METHODS AND MATERIALS

Turbine Blade Geometry

For generating electric power, the blades, which are the main elements of a hydrokinetic turbine as mentioned previously, are connected to a central hub and rotate with it, producing electric power from the shaft [1, 5]. The part of the blade farthest from and closest to the hub are named the blade tip and the blade root, respectively. The hydrofoil stands for the blade cross-section perpendicularly drawn to the imaginary line linking the blade root to the tip. The shape of the hydrofoil is involved in the production of a lift coefficient by creating suction on the hydrofoil upper surface [2, 5]. While this process is occurring, a drag is also produced, which is an undesirable phenomenon for the hydrokinetic turbine output power maximization tasks. Therefore, in order to achieve the maximum power output and torque from a hydrokinetic turbine with horizontal-axis, the generation of high C_L and C_L/C_D values are of utmost importance, being the hydrofoil design a crucial parameter. It is noteworthy that C_L is a dimensionless number that evaluates the capability of the hydrofoil for generating lift. This coefficient is defined by Eq. (1) [2]:

$$C_L = \frac{L}{\frac{1}{2}\rho V^2 S} \tag{1}$$

where ρ and V are the fluid density and velocity, respectively; S refers to the hydrofoil surface; and L is the lift force. In turn, C_D can be calculated using Eq. (2) [2]:

$$C_D = \frac{D}{\frac{1}{2}\rho V^2 S} \tag{2}$$

where D is the drag force or the force component in the direction of the flow velocity.

During the first stages of the design process, the selection of a proper hydrofoil is highlighted [2] due to the blades of traditional hydrokinetic turbines should create lift [2], whose value is influenced by the blade hydrofoil and the chord length (C). Considering that multiple-hydrofoils conform the turbine blade, several lifts are generated according to the number of hydrofoils, resulting in the lift of the entire blade [8]. In applications requiring strong lift forces, as hydrokinetic turbines with large α and reduced flow velocities, the traditional hydrofoil profiles tend to produce flow separation near the trailing edge, generating vortices and decreasing the profile efficiency [22, 23].

The multi-element profiles are often an appropriate solution increasing the lifting force, allowing a greater curvature for a high α operation and delaying the separation of the flow close to the trailing edge [16]. This delay in the separation of the flow at the blade is achieved by introducing a slat in front of the trailing edge of the blade or a flap behind it for the control of the boundary layer [16]. Nevertheless, the parameters of multi-element profiles should be appropriately adjusted, including the width of the space between the element and the orientation of each adjacent element for the given conditions [24, 25] so that the efficiency increase is possible.

As illustrated in Figure 1, several configurations might exist for a multi-element blade design. As observed, the combination of slats and flaps around a main hydrofoil element is possible to be performed in order to obtain an optimal profile with the maximum C_L.

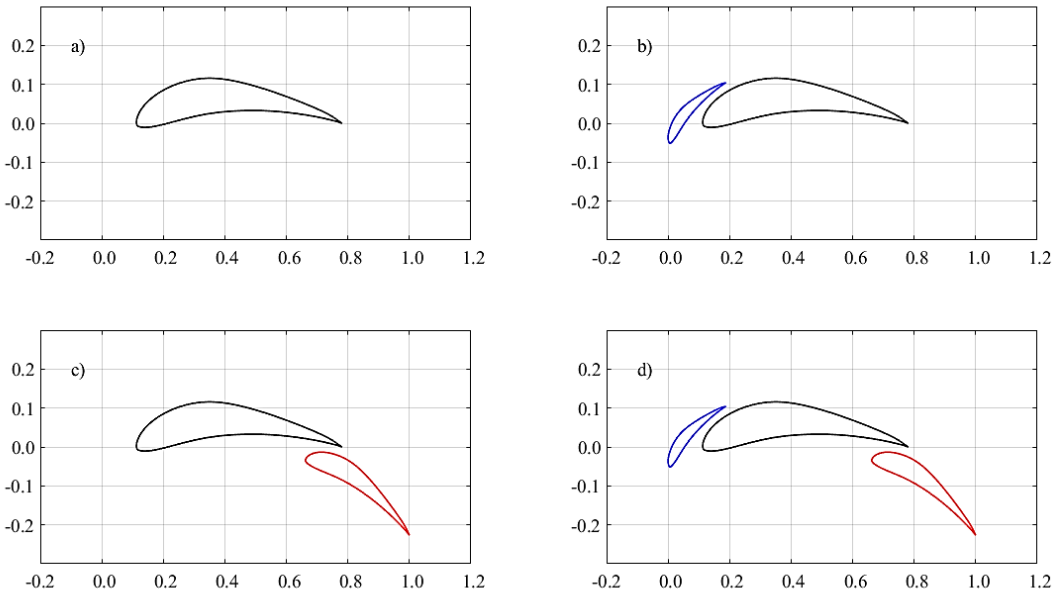

Figure 1. Geometry of a multi-element hydrofoil: (a) main element, (b) main element with slat, (c) main element with flap and (d) main element with slat and flap [26]

Hydrofoil Cross-section Design and Optimization by using JavaFoil Code

To design a high-performance rotor of a hydrokinetic turbine of 1 kW with a multi-element blade, a detailed numerical study was performed by using JavaFoil code [26]. Initially, for the design of the multi-element profile represented in Figure 2, the guidelines reported by Narsipur and coworkers were followed [16]. According to the authors, the length of the second element (flap), the vertical space (*d*), the horizontal space (*h*) between the trailing edge of the main element and the leading edge of the second element, δ and α must be 30%C_1, from 2 to 3%C_1, close to 5.3%C_1, between 20 and 50°, and between -5 and 20°, respectively. It is important to note that δ refers to the angle between the flap chord and the main element chord.

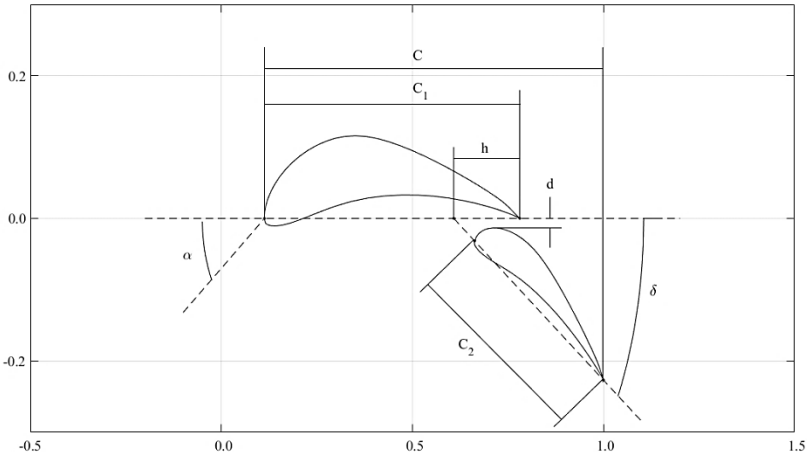

Figure 2. Multi-element hydrofoil configuration [28]

By using JavaFoil code, 14 multi-element and 14 traditional hydrofoil configurations were analyzed. The profiles analyzed were S805, S822, Eppler 857, CH 10-48-13, Eppler 420, Eppler 421, Eppler 422, Eppler 423, Wortmann FX 74-CL5-140, Wortmann FX 74-CL5-140 MOD, Douglas/Liebeck LA203A, Selig S1210, Selig S1223 and UI-1720. In this work, only the effects of the flap length and δ were investigated on such configurations in order to quantify the change in C_L and C_D for the multi-element hydrofoil studied. The profiles were analyzed for a Reynolds number (*Re)* equal to 750000, which is considered as a characteristic *Re* for hydrokinetic turbines. Additionally, *C* remained equal to 1 in traditional and multi-element configuration profiles. Furthermore, C_L and C_D were analyzed every 1° in a wide range of α. This procedure was followed for the whole set of the analyzed profiles.

In order to calculate these coefficients for a given flow condition (α and *Re*), JavaFoil code combines a potential flow panel method and an integral boundary layer formulation. The procedure used consisted of the following stages. a) First, the velocity distribution on the hydrofoil surface is calculated by using a potential flow analysis module based on a higher order panel method. b) The pressure distribution is integrated along the hydrofoil surface to obtain the pitching moment coefficient and the lift. c) Afterwards, the boundary layer behavior is calculated using the boundary layer analysis module, enabling to find the boundary layer parameters by solving a set of differential equations. d) Finally, the hydrofoil drag is calculated from the obtained boundary layer data.

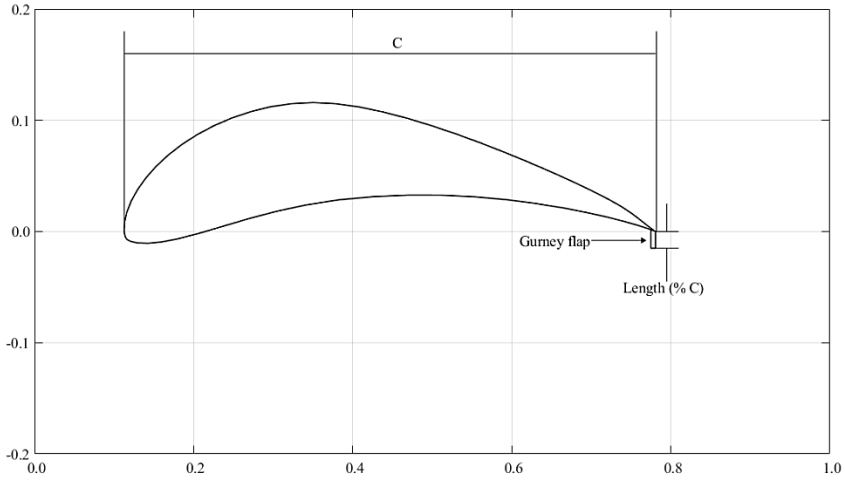

Figure 3. Hydrofoil with a Gurney flap

It is important to note that JavaFoil code offers good results when compared to experimental results and other numerical analysis tools [27]. The Gurney flap constitutes another mechanical simple way to increase the hydrofoil C_L. It is defined as defined as a flat plate located perpendicularly to the hydrofoil pressure side at the trailing edge [28], as shown in Figure 3. When properly sized, the Gurney flap will increase the total lift of the hydrofoil while reducing the drag. Bianchini and coworkers conducted CFD to perform numerical analyses in order to evaluate the potential of using Gurney flaps for the power augmentation of a Darrieus wind turbine. Two length values of the Gurney flap were studied by the authors, corresponding to 1% and 2%*C* [21]. On the other hand, Jain et al. analyzed the effect of the Gurney flap

on airfoil aerodynamics using ANSYs Fluent software. Six different Gurney flap lengths, from 0.5% to 4%C, were used for 2D computational investigation. The influence of the Gurney flap length on the best hydrofoil with and without multi-element configuration previously analyzed with a high C_L/C_D was also numerically investigated by using JavaFoil code. Under this scenario, in the current study, Gurney flap sizes of 1%, 2%, 3%, 3.5% and 4%C were studied.

Fluid Dynamics and Structural Analyses

The sizing of other components that are part of the hydrokinetic turbine was processed once the best profile was selected. For this purpose, the blade element theory was used [5]. A hydrokinetic turbine of 1 kW was designed for 1.5 m/s of a free stream water velocity (V) and 6.325 of tip speed ratio (λ), a water density (ρ) of 997 kg/m^3 (at 25°C), an initial α and pitch angle (θ) of 5 and 0°, respectively, a drive train efficiency (η) of 70%, and a power coefficient (C_p) of 0.4382 [5]. It is highlighted that λ refers to the ratio between the tangential speed of the blade tip and V. In turn, θ and C_p stand for the angle formed by the chord of the profiles and the blade rotation plane, and the ratio between the energy captured by the turbine and the kinetic energy available in the free stream water, respectively.

It is important to note that the design power of 1 kW was chosen due to the rivers of developing countries rarely flow at a velocity higher than about 1 m/s. In addition, they are not deep enough for horizontal-axis hydrokinetic turbines greater than about 2 m of diameter are immersed [29, 30]. The power output (P) of a horizontal-axis hydrokinetic turbine was calculated using Eq. (3), where A is the area swept by the rotor blade ($A = \pi R^2$) and R refers to the rotor radius or the blade length [5].

$$P = \frac{1}{2}\rho A V_1^3 \, C_P \eta \tag{3}$$

Therefore, if P is equal to 1 kW, then the turbine rotor diameter is 1.58 m. In this regard, the rotor of the turbine has 3 blades of R equal to 0.79 m. It should be noticed that 3-bladed turbines are characterized by their higher stability and reduced vibration, with the subsequent reduction of fatigue failures owing to the rise in their bearing life [5, 31]. Additionally, turbines with 3 blades exhibit a lower λ compared to turbines with 2 blades, leading to the reduction of cavitation inception chances [32]. In this study, the blades were developed with the best hydrofoil (Eppler 420) with and without a multi-element configuration.

The twist distribution angle (β) and C are presented in Figure 4. C of a blade element can be calculated by Eq. (4). In turn, β at any point along the blade can be calculated as represented by Eq. (5). Eq. (4) and Eq. (5) depend on the number of blades (B), α, C_L and C_D of the Eppler 420 hydrofoil selected, the local point along the blade (r), the angle of the relative water current to the plane of rotation (ϕ), the axial flow induction factor (a), the local tip speed radio (λ_r) and the angular induction factor (a') [2, 5]. ϕ, a, λ_r and a' can be obtained from Eq. (6) to Eq. (9), respectively. It is important to note that a must be less than 0.5 for the the moment theory can be applied.

$$C = \frac{8a'r\lambda_r \pi Sin^2\phi}{(C_L Sin\phi - C_D Cos\phi)B(1-a)} \tag{4}$$

$$\beta = \phi - \alpha \tag{5}$$

$$Tan\phi = \frac{(1-a)}{\lambda_r(1+a')} \tag{6}$$

$$C_p = \frac{4a(1-a)^2}{\eta} \tag{7}$$

$$\lambda_r = \frac{\omega r}{V} = \lambda \frac{r}{R} \tag{8}$$

$$\frac{a(1-a)}{a'(1+a')} = \lambda_r^2 \tag{9}$$

After having found C and β values for each section, the chord values were multiplied by the non-dimensional coordinates of the Eppler 420 profile.

SolidWorks software was used to export the profile x and y coordinates for every section along the blade. Thus, the blade cross-sections were obtained from the root to the tip for several distances. Finally, a blade 3D-model was achieved by utilizing the Loft command [33]. In Figure 5 the resulting image is represented. During the process, the first section near the blade root was removed and the second section of the blade profile was modeled with the same β of the third section. Furthermore, for the blade structural strength improvement, a corrective factor (F_c) or geometric scale equal to 17.1 was introduced. Therefore, each previously calculated chord length was multiplied by this F_c. The blade model also includes a rectangular transition area from the steel hub to the first station of the blade.

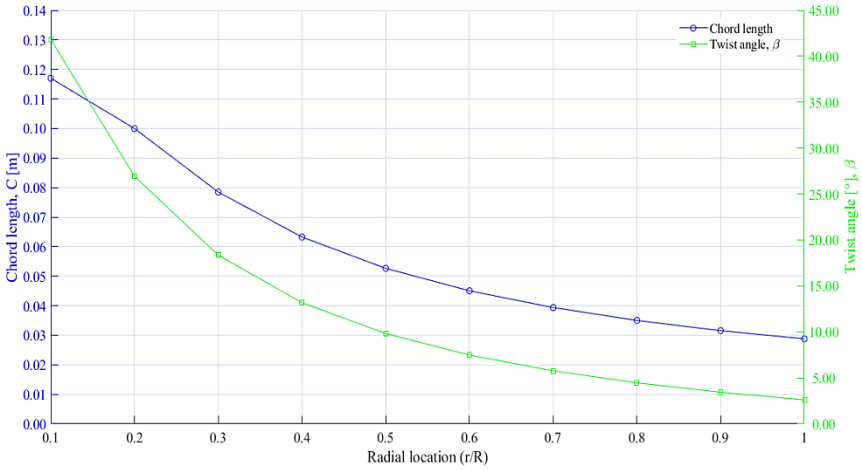

Figure 4. Radial location of the chord length (C) and the twist angle (β) along the blade

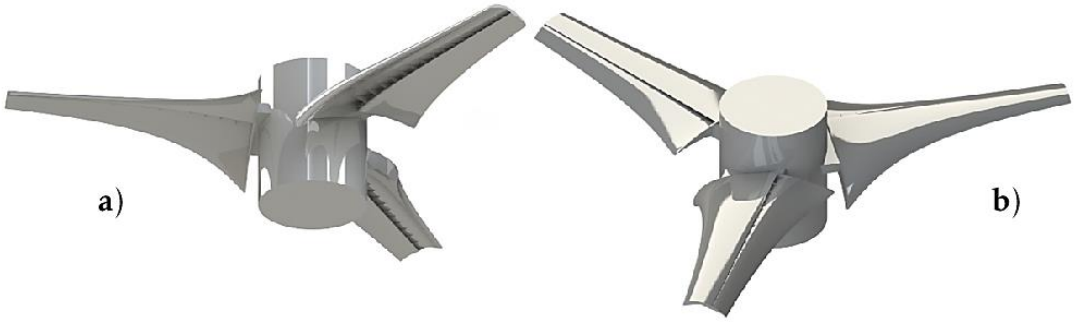

Figure 5. 3D model of the hydrokinetic turbine of 1 kW

A complete 3D CFD analysis was carried out for the validation of the obtained rotor hydrodynamic design with the aid of ANSYs Fluent software version 17.0. Simulation was conducted using a sector of the rotor formed of one blade and 120° of angle, considering the features ascribed to the cyclic symmetry of the hydrokinetic turbine rotor structure. The dimensions of the computational domain, which was generated by using SolidWorks software, were provided in terms of R, as represented by Figure 6. The rotation plane of the turbine was located $2R$ of the inlet. In order to take the remote wake effect, behind the plane of the turbine, the fluid domain was extended $5R$.

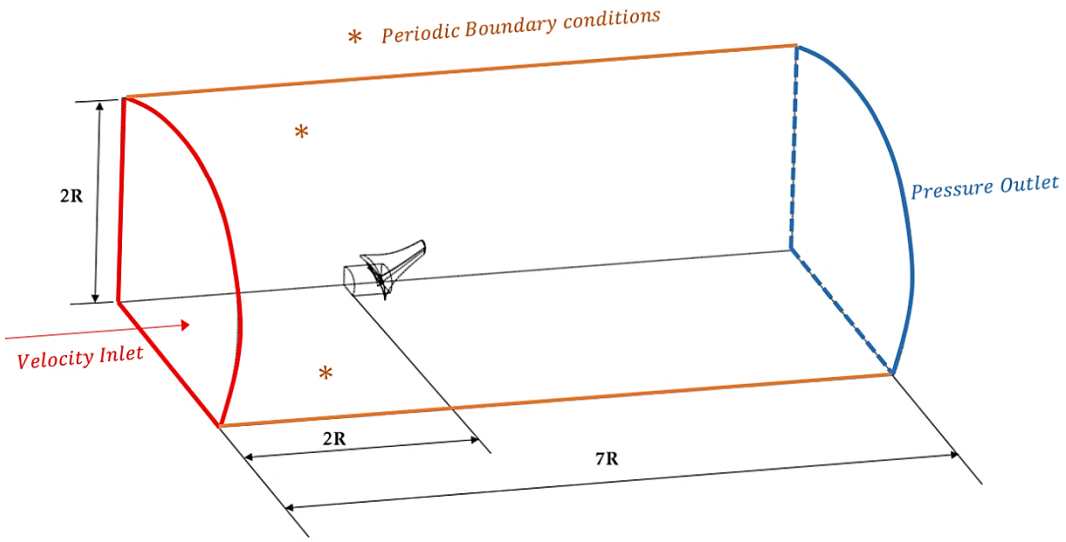

Figure 6. Computational domain used for CFD analysis

The study assumes steady regime and incompressible flow. For flow simulations, RANS model, which stands for the Reynolds-Averaged Navier-Stokes model, was utilized. Correspondingly, as illustrated in Figure 6, for the domain left surface, 1.5 m/s uniform velocity inlet was provided as the boundary condition in the normal left face. In turn, in the right surface, a zero-gauge pressure was applied as the pressure output limit condition. Additionally, across the computational domain back and bottom surface, a rotational periodic boundary condition was implemented with a rotation velocity of 12.009 rad/s. On the other hand, Shear Stress Transport (SST) $k - w$ turbulence model was chosen due to its accuracy for flows exhibiting detrimental adverse pressure gradients [34], as it is the current case. This model has been successfully used by several authors [27, 35, 36]. 5% of turbulence intensity was also set. Moreover, 0 m/s was applied as the blade and the hub relative speed values. Therefore, the no-slip condition was established either for the blade or the hub of the turbine. Details of the simulation variables used are listed in Table 1.

Table 1. Parameters involved in the CFD analysis

Parameters	Value
Hydrofoil	Eppler 420
Density (ρ)	997 kg/m^3
Number of blades	3
Velocity inlet	1.5 m/s
Pressure outlet	Zero gauge pressure
Blade and hub walls	No-slip condition
Rotor speed	12.009 rad/s
Turbulence model	$k - w$ SST
Turbulence intensity	5%
Interpolating scheme	2nd order upwind
Pressure scheme	PRESTO
Residual error	1x10^{-6}

The computational domain was meshed using ANSYs Fluent software. An unstructured tetrahedral mesh with a layer of very thin elements near the walls of the turbine blade was used. To capture the boundary layer near the blade walls, a prism layer was grown from the blade surface. A closer grid view in the hydrofoil vicinity is represented in Figure 7. In order to find an appropriate boundary layer resolution close to the trailing edge and the hydrofoil surface, a grid clustering is required. Such as grid clustering was also needed to obtain a proper resolution of the region surrounding the Gurney flap.

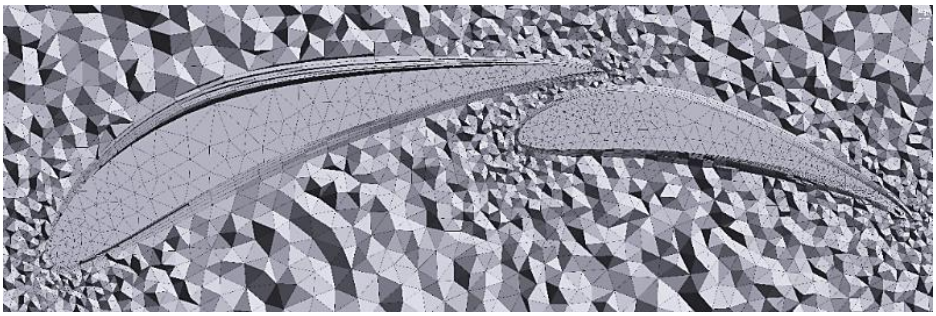

Figure 7. Mesh used for CFD analysis

It must be noted that the highest gradient of static pressure and velocity are located in a region around the blade. Therefore, this region plays a crucial role on the hydrokinetic turbine performance [37]. In addition, the wake flow has a great effect on the power [38, 39]. The wake can extend up to downstream the blade. During the computational fluid dynamics analysis of this phenomenon around the hydrokinetic turbine, the desired accuracy and solution costs depend on the mesh geometry domain. Turbulent flows are widely known to be influenced by the walls, where the regions affected by the viscosity exhibit high gradients in the solution. The successful prediction of the turbulent flow around the blade wall is determined by the near-wall region accurate meshed. In this regard, a refinement in the boundary layer and a sensitivity study of $y+$ are very important, since both of them can affect the turbine hydrodynamics. $y+$ is a non-dimensional distance utilized in CFD for describing how coarse or fine is a mesh. It refers to the ratio between the effect

of a turbulent flow and a laminar one on a particular cell [40]. $y+$ is defined by Eq. (10), being Δy, $u+$ and v the first node distance from the wall, the wall shear velocity and the kinematic viscosity, respectively.

$$y^+ = (\Delta y u^+ / v) \tag{10}$$

Therefore, three layers can be obtained from the rough subdivision of the near-wall region: the viscous sublayer ($y+ < 5$), the blending region or the buffer layer ($5 < y+ < 30$) and the low region or the fully turbulent layer ($y+ > 30$ to 60) [41]. In general, for wall functions and near-wall modeling, $y+ \approx 30$ and $y+ \approx 1$ are regarded as the most desirable values, respectively. In order to evaluate the effect of the number of elements in the computational fluid dynamics analysis, a study of the mesh independence was conducted, as observed in Table 2. Therefore, by augmenting the near wake refinement, 6 meshes were generated. A boundary layer appropriate resolution was found. For assuring the solution convergence, the torque on the blade was controlled. The mesh 6, which consisted of 7738124 elements and 3381663 nodes, provided the convergence of the results with an error of 0.389% on the torque. Consequently, the obtained numerical results might not be improved by a further mesh refinement. Additionally, a steady-state condition was assumed for the simulation using approximately 2000 iterations. A decrease of at least 6 orders of magnitude in the scaled residuals of the achieved CFD solution values was considered for convergence. As illustrated in Figure 8, utilizing the $k - w$ SST turbulence model, the final mesh had a $y+ < 5$. This result allowed achieving the solution of the laminar sub-layer.

Table 2. Mesh convergence study

Mesh	Nodes	Elements	$y+$	Torque	Error %
Mesh 1	543704	1660605	18.915	143.189	3.231
Mesh 2	789489	2836275	34.794	138.707	3.130
Mesh 3	937017	3064066	23.881	138.139	0.409
Mesh 4	1169225	3471202	13.725	143.860	4.141
Mesh 5	2085542	6118335	10.685	142.263	1.110
Mesh 6	3381663	7738124	1.901	142.816	0.389

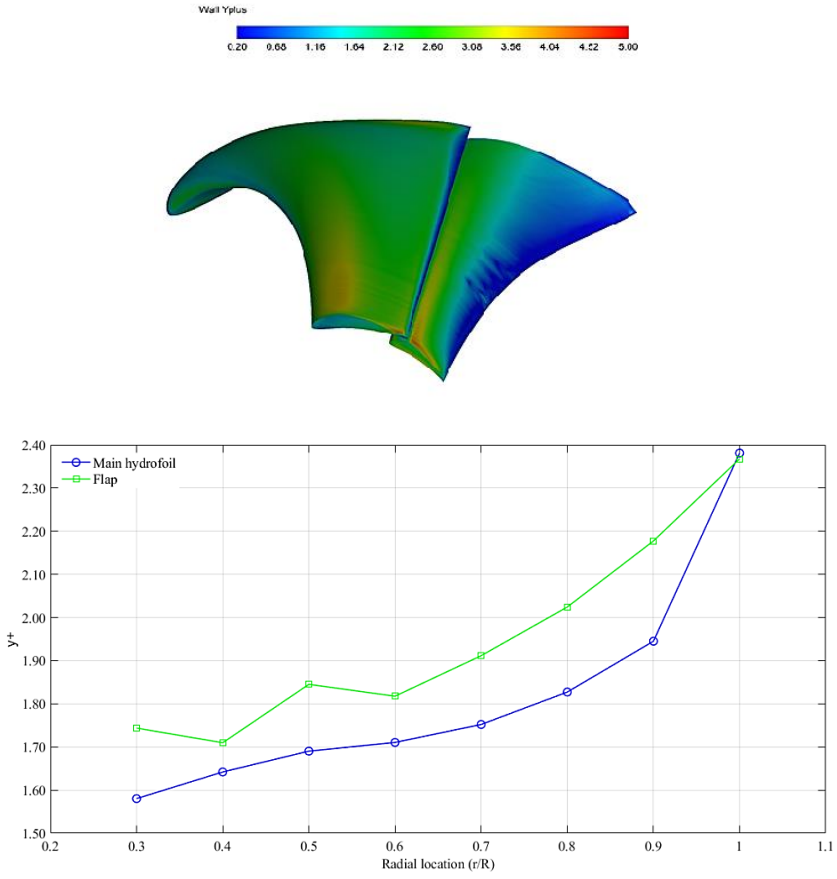

Figure 8. y^+ on the hydrofoil

Furthermore, the structural design of the rotor was also validated with a detailed 3D fluid-structure interaction analysis using ANSYs Fluent software. The structural and fluid domains were connected by using one way coupling. Subsequently, the analysis of a fluid-structure interaction was performed for obtaining the influence of experimental conditions and the geometry of the blade on the stresses developed. In this regard, the hydrokinetic turbine blades were analyzed under hydrodynamic, centrifugal and gravitational loads that the turbine may experience during its operating life.

Fluid Structure Interaction system was created for determining hydrodynamic loads associated with extreme flow conditions and performing static analyses throughout the use of the blade pressure loads from Fluent software. Additionally, mapping algorithm and the Static analysis module were used for transferring and projecting the pressure loads on the surface geometry of the blade, respectively, considering that in Fluent module the blade geometry position is equal to that of the Static Structural module concerning the global coordinate system.

In the set-up of ANSYs Static Structural module, the gravity and the centrifugal load, which was placed at 12.009 rad/s rotation velocity, were also defined. By fixing all the degrees of freedom at the hub, the models of the analyzed blades were considered as a cantilever beam. In addition, two materials, aluminum (6061-T6) and AISI 304 steel, were used for the numerical analyses. The mechanical properties of the materials considered for the structural analysis are presented in Table 3.

Table 3. Mechanical properties of the materials used for the blade

Material	Elastic Modulus [GPa]	Density [kg/m^3]	Poisson ratio	Tensile strength ultimate/Yield [MPa]
Aluminum (6061-T6)	69	2700	0.33	310/276
AISI 304 Steel	193	8000	0.30	305/215

In general, the processes described in this work are presented in Figure 9. The framework is made of three different parts to analyze the hydrofoils in order to know their characteristics and performance: a) a main 2D analysis using JavaFoil code in order to select the best multi-element high-lift hydrofoil for the design of the blades of hydrokinetic turbines, b) a 3D CFD analysis for validating the hydrodynamic behavior of the blade design and c) a 3D Finite Element Analysis to validate the blade structural performance.

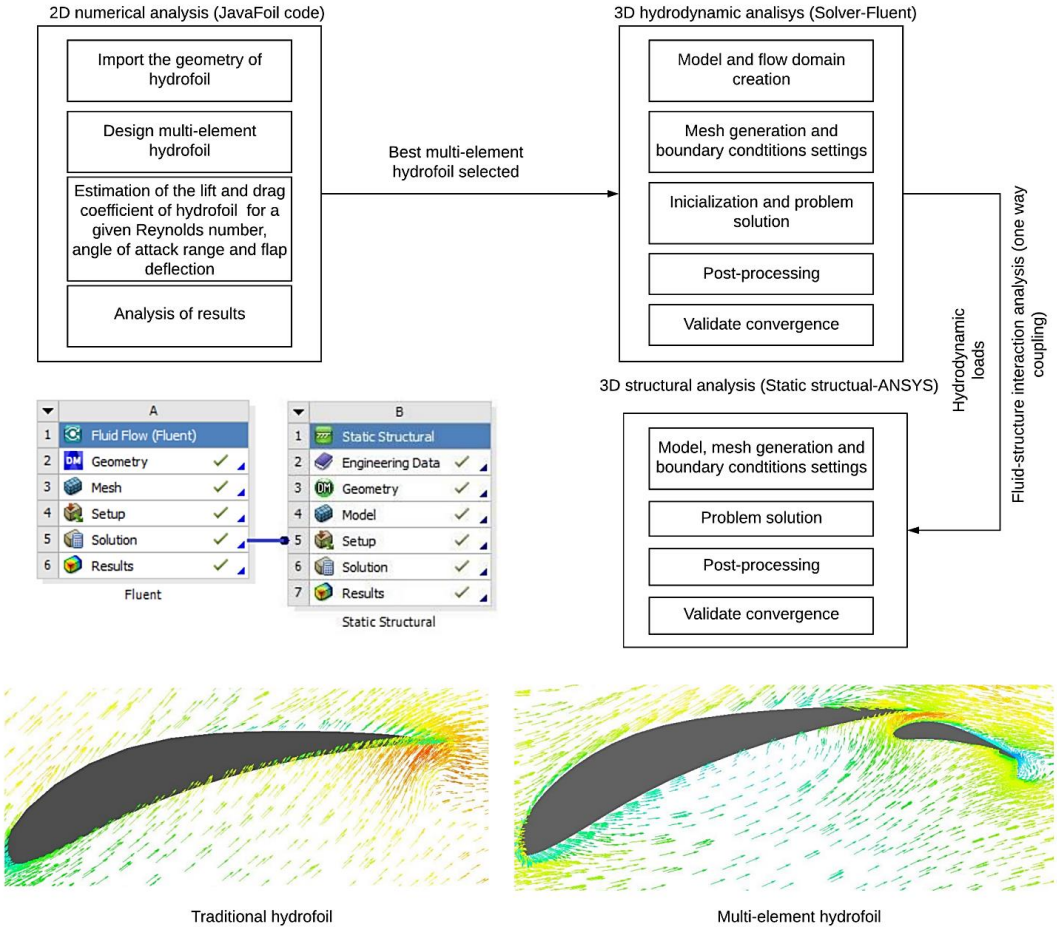

Figure 9. Framework used for the blade design

RESULTS AND DISCUSSION

Analysis of a Hydrofoil with a Traditional and a Multi-element Configuration

After having conducted repeated comparative studies between 14 multi-element and 14 traditional hydrofoil configurations, the obtained C_{Lmax}, C_{Lmax}/C_D, α and δ values calculated using JavaFoil code are compiled in Table 4. As it can be observed, the multi-element hydrofoil configurations caused a significant improvement of the hydrofoil hydodynamic performance. This result was supported by several experimental and numerical studies found in the literature [12-17, 24].

From the results, the best profiles resulted to be the Eppler 420 and the Selig S1223 multi-elements with α and δ values equal to 8° and 30°, and 3° and 10°, respectively. The Selig S1223 multi-element had a C_{Lmax} (3.84) higher than that of the Eppler 420 multi-element (3.69). However, the Eppler profile had a higher C_{Lmax}/C_D (47.77) compared to that of the Selig profile (39.59), as illustrated in Figure 10. In addition, the Eppler profile is thicker and capable of supporting higher hydrodynamic loads during its operation. Therefore, this profile was chosen for the blade design of the 1 kW hydrokinetic turbine. In Figure 11, C_L and C_D for the Eppler 420 traditional and multi-element hydrofoils are compared. Reza and coworkers also compared the traditional airfoil Eppler 420 and Selig S1223 for aerodynamic applications. The analysis was carried out considering standard values of wing area (1.2 m^2), relative wind speed (40 km/h) and R_e (450000) for conventional low speed unmanned aero vehicles. As in the current study, the obtained results by the referred authors showed that the Selig S1223 profile had a C_{Lmax} (2.36) higher than that of the Eppler 420 (2.16). Additionally, the Eppler profile had a higher C_{Lmax}/C_D (152.14) compared to that of the Selig profile (112.38) [42].

Table 4. Performance of hydrofoils

Hydrofoil	α	δ	$C_{L_{max}}$	$C_{L_{max}}/C_D$
S805	11	-	1.32	38.25
S805 multi-element	6	20	1.74	31.85
S822	12	-	1.42	35.20
S822 multi-element	7	20	1.85	38.18
Eppler 857	18	-	2.08	19.50
Eppler 857 multi-element	9	25	3.04	33.76
Selig S1210	10	-	2.33	58.00
Selig S1210 multi-element	2	35	3.21	45.83
CH10	13	-	2.36	34.51
CH10 multi-element	4	25	3.20	42.13
Eppler 420	17	-	2.57	24.47
Eppler 420 multi-element	8	30	3.69	47.77
Eppler 421	17	-	2.28	23.37
Eppler 421 multi-element	8	25	3.21	38.88
Eppler 422	17	-	1.97	20.75
Eppler 422 multi-element	7	20	2.71	62.17
Eppler 423	15	-	2.45	30.18
Eppler 423 multi-element	6	30	3.39	48.63
Wortmann FX 74-CL5-140	13	-	2.30	27.26
Wortmann FX 74-CL5-140 multi-element	5	30	3.40	93.32
Wortmann FX 74-CL5-140 MOD	12	-	2.26	32.51

Hydrofoil	α	δ	$C_{L_{max}}$	$C_{L_{max}}/C_D$
Wortmann FX 74-CL5-140 MOD multi-element	3	30	3.21	42.28
Douglas Liebeck LA203A	18	-	2.17	23.22
Douglas Liebeck LA203A multi-element	9	30	3.09	33.92
Selig S1223	12	-	2.80	49.41
Selig S1223 multi-element	3	10	3.84	39.59
UI-1720	19	-	1.72	12.70
UI-1720 multi-element	11	20	2.27	22.60

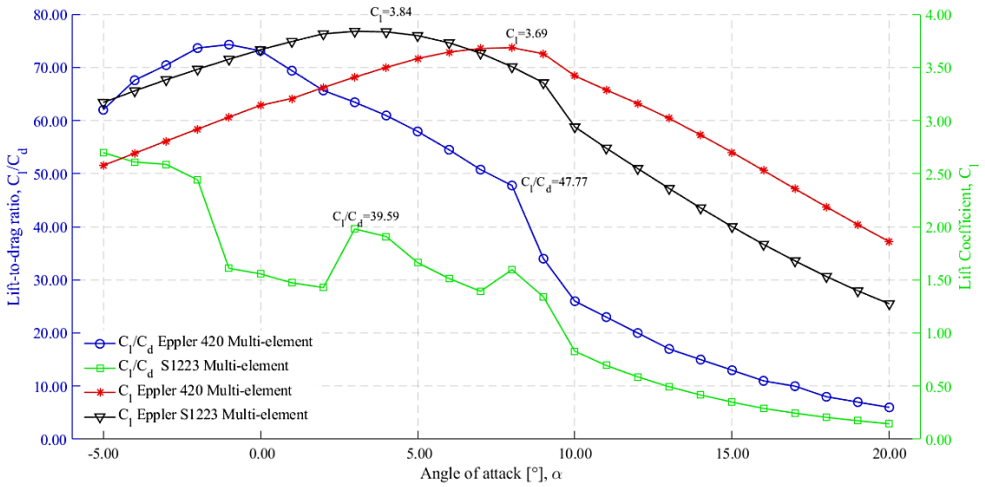

Figure 10. Comparison between the Eppler 420 multi-element and the Selig S1223 multi-element hydrofoils

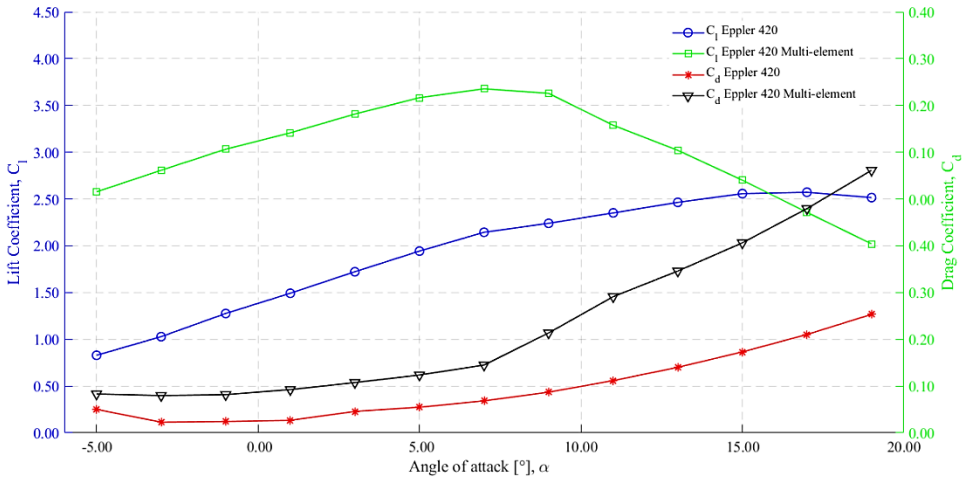

Figure 11. Comparison between the lift and drag coefficients (C_L and C_D, respectively) for the Eppler 420 traditional and the Eppler 420 multi-element hydrofoils

Influence of the Gurney flap on a Hydrofoil with and without a Multi-element Configuration

The Eppler 420 traditional and multi-element hydrofoils were the geometries utilized for studying the Gurney flap. A Gurney flap size range from 1 to 4%*C*, with the flaps placed on the main profile back edge, was used for computations. The results obtained from JavaFoil code are compiled in Table 5. In most cases, it can be observed that the hydrofoils with a Gurney flap result in a C_{Lmax} and a C_{Lmax}/C_D increase and decrease, respectively, when α is decreased. The numerical results show an increase in efficiency when a gurney flap is used [43, 44].

A Gurney flap of 4% and 3.5%C was selected for the traditional and the multi-element hydrofoil, respectively. In the literature, the effect of Gurney flaps have been widely studied for lift enhancement in aircraft applications; as well as on the aerodynamic performance of wind turbines, especially the Darrieus wind turbine [43, 44]. For example, Bianchini and coworkers investigated the effect of Gurney flaps on a Darrieus turbine designed with the airfoil NACA0021. The results showed than the best configuration of the hydrofoil with a Gurney flap resulted in a Gurney flap length of 2%C [21]. On the other hand, Jain et al. conducted a numerical simulation on NACA 0012 airfoil. The study concluded that the Gurney flaps with a size of 1.5%C must be installed perpendicularly to the chord and as close to the trailing edge as possible to obtain the maximum lift enhancement with minimum drag penalty [45]. The optimal Gurney flap length varies for different airfoils, which means that a fixed Gurney flap length would not reach the optimal C_{Lmax}/C_D. Therefore, this result suggests that a careful analysis of the Gurney flap length is needed for each airfoil or hydrofoil and multi-element configuration. In conclusion, the Gurney flap was observed to provide a lift improvement and a drag reduction once it was properly sized.

Table 5. Performance of several Eppler 420 hydrofoil configurations

Hydrofoil	α	$C_{L_{max}}$	$C_{L_{max}}/C_D$
Eppler 420	17	2.57	24.47
Eppler 420 with a Gurney flap of 1.0%C	16	2.61	23.18
Eppler 420 with a Gurney flap of 2.0%C	16	2.71	22.32
Eppler 420 with a Gurney flap of 3.0%C	15	2.78	22.02
Eppler 420 with a Gurney flap of 4.0%C	15	2.82	19.20
Eppler 420 with a multi-element configuration	8	3.69	46.12
Eppler 420 with a multi-element configuration and a Gurney flap of 1.0%C	7	3.74	45.65
Eppler 420 with a multi-element configuration and a Gurney flap of 2.0%C	7	3.84	42.81
Eppler 420 with a multi-element configuration and a Gurney flap of 3.0%C	7	3.84	39.48
Eppler 420 with a multi-element configuration and a Gurney flap of 3.5%C	7	3.85	39.48
Eppler 420 with a multi-element configuration and a Gurney flap of 4.0%C	7	3.20	28.90

Effect of the Flap Length

The influence of the flap length of the Eppler 420 multi-element hydrofoil on C_L and C_D was studied. The data found by using JavaFoil code are listed in Table 6. It can be observed that the most appropriate length of the flap was identified to be 70%C_1 with a α value equal to 0º, which implies a low C_D and a high C_L.

Table 6. Flap length influence on the Eppler 420 multi-element hydrofoil performance [46]

Flap length	40%		50%		60%		70%		80%	
α	$C_{L_{max}}$	C_D	$C_{L_{max}}$	C_D	$C_{L_{max}}$	C_D	$C_{L_{max}}$	C_D	$C_{L_{max}}$	C_D
-5	2.80	0.04	3.04	0.04	3.22	0.04	3.38	0.04	3.51	0.05
-4	2.91	0.04	3.15	0.04	3.33	0.04	3.49	0.05	3.62	0.05
-3	3.03	0.04	3.26	0.04	3.44	0.05	3.60	0.05	3.72	0.06
-2	3.14	0.04	3.37	0.04	3.55	0.05	3.70	0.06	3.82	0.06
-1	3.25	0.04	3.48	0.05	3.65	0.05	3.80	0.06	3.89	0.07
0	3.36	0.04	3.58	0.05	3.75	0.06	3.86	0.06	3.93	0.07
1	3.39	0.05	3.61	0.06	3.74	0.06	3.80	0.07	3.83	0.08
2	3.49	0.05	3.69	0.06	3.79	0.07	3.81	0.07	3.81	0.08
3	3.58	0.06	3.74	0.06	3.82	0.07	3.79	0.08	3.76	0.08
4	3.66	0.06	3.77	0.07	3.81	0.08	3.73	0.08	3.67	0.09
5	3.72	0.06	3.77	0.07	3.78	0.08	3.64	0.09	3.56	0.10

Flap length	40%		50%		60%		70%		80%	
6	3.75	0.07	3.74	0.08	3.72	0.09	3.52	0.14	3.40	0.16
7	3.76	0.07	3.67	0.12	3.62	0.14	3.37	0.16	3.16	0.20
8	3.74	0.08	3.57	0.13	3.48	0.15	3.10	0.19	2.96	0.21
9	3.65	0.13	3.32	0.16	3.21	0.18	2.91	0.21	2.78	0.23
10	3.40	0.15	3.15	0.18	3.03	0.20	2.72	0.23	2.59	0.25
12	3.11	0.18	2.80	0.21	2.67	0.23	2.36	0.27	2.24	0.29
14	2.78	0.21	2.44	0.24	2.31	0.27	1.97	0.32	1.92	0.35
15	2.61	0.23	2.27	0.26	2.14	0.30	1.81	0.34	1.78	0.38
16	2.44	0.24	2.10	0.28	1.97	0.32	1.66	0.37	1.64	0.41
18	2.09	0.29	1.78	0.34	1.63	0.38	1.45	0.44	1.34	0.48
19	1.93	0.31	1.63	0.37	1.54	0.41	1.32	0.47	1.23	0.51
20	1.78	0.34	1.49	0.40	1.41	0.45	1.22	0.50	1.13	0.55

CFD Analysis Results

Simulations from CFD allow obtaining the pressure distribution on the blade, as well as the flow field within the computational domain, as represented in Figures 12-16, in a cross-section of the blade located at 0.5*R* from the hub. Five geometries (geometry A, B, C, D and E) were studied. Geometry A and B consisted of solid blades with an Eppler 420 hydrofoil without and with a Gurney flap of 3.5%*C*, respectively. In turn, geometry C and D were generated by using solid blades with an Eppler 420 multi-element hydrofoil 30%C_1 without and with and a Gurney flap of 3.5%*C*. Finally, geometry E consisted of a solid blade with an Eppler 420 multi-element hydrofoil 70%C_1. The pressure distribution and the flow field were visualized and analyzed in the wake region in order to understand the complex flow field near the trailing edge and between the main element and the flap in multi-element configurations.

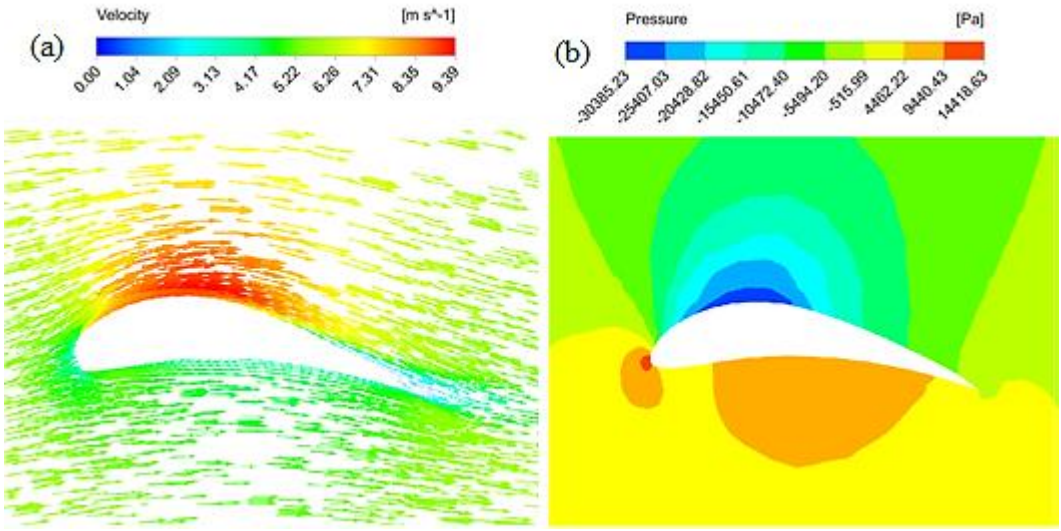

Figure 12. Geometry A- solid blade with an Eppler 420 hydrofoil: (a) flow field and (b) pressure distribution on the plane located at 0.5*R* from the hub

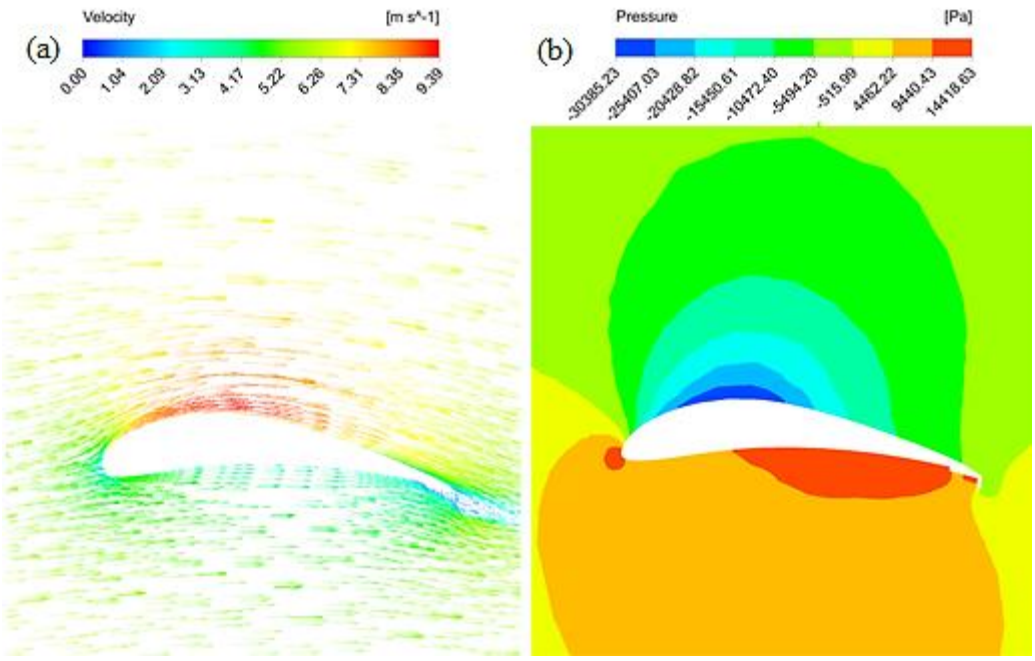

Figure 13. Geometry B- solid blade with an Eppler 420 hydrofoil and a Gurney flap of 3.5%*C*: (a) flow field and (b) pressure distribution on the plane located at 0.5*R* from the hub

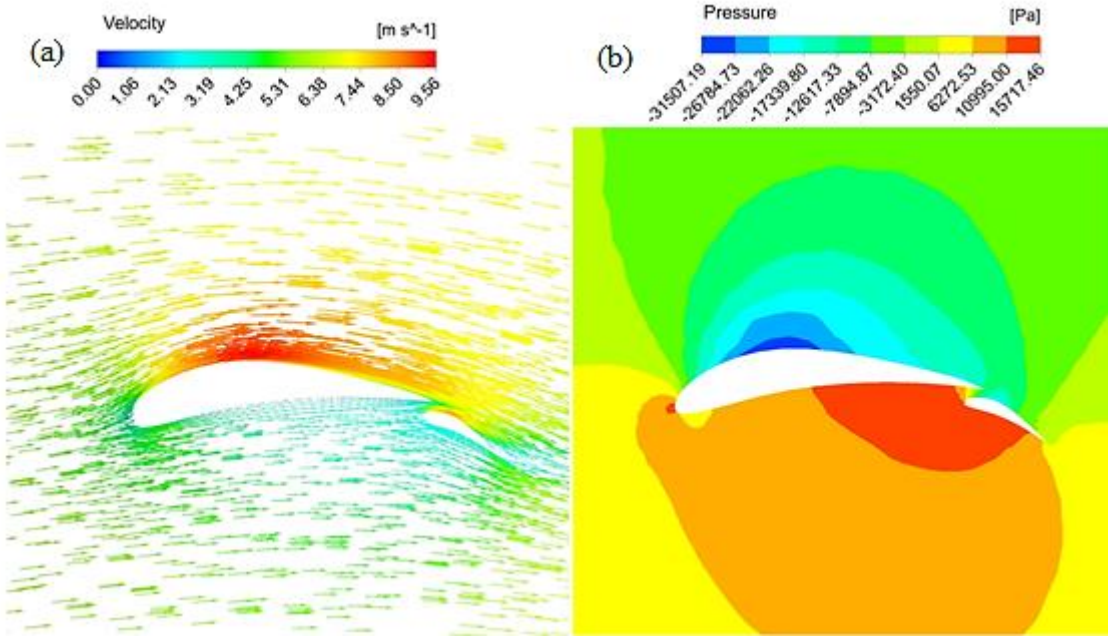

Figure 14. Geometry C- solid blade with an Eppler 420 multi-element hydrofoil of 30%C_1: (a) flow field and (b) pressure distribution on the plane located at 0.5*R* from the hub

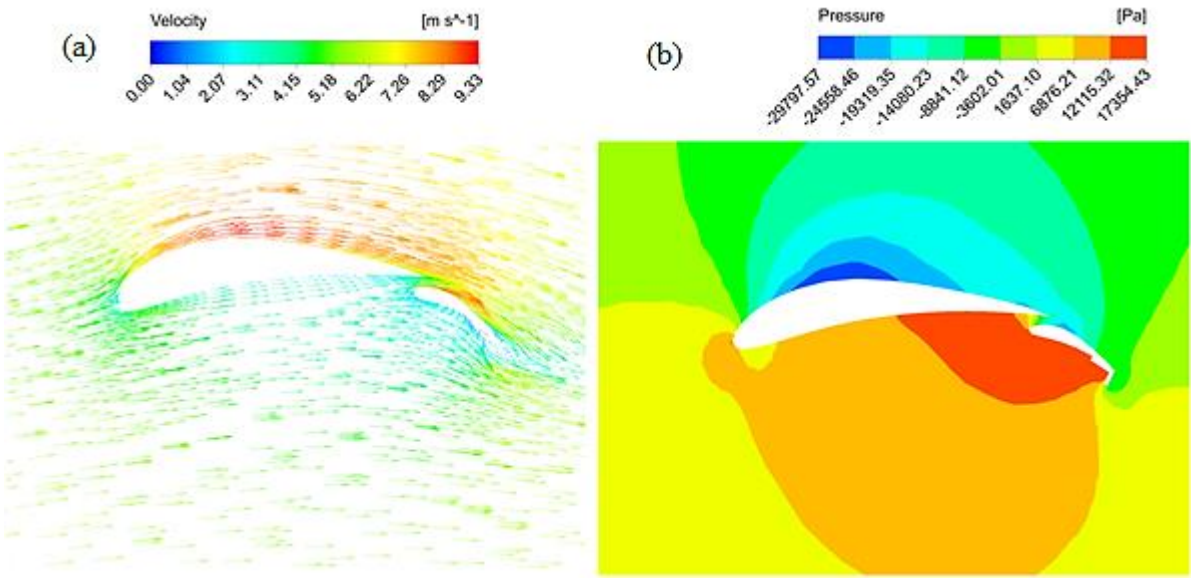

Figure 15. Geometry D- solid blade with an Eppler 420 multi-element hydrofoil of 30%C_1 and a Gurney flap of 3.5%C: (a) flow field and (b) pressure distribution on the plane located at 0.5R from the hub

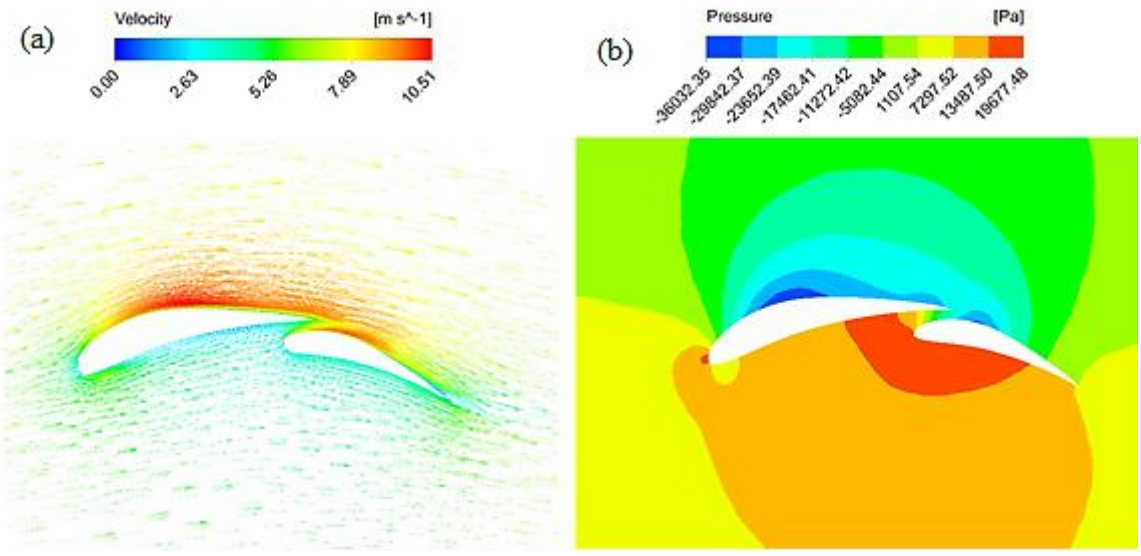

Figure 16. Geometry E- solid blade with an Eppler 420 multi-element hydrofoil of 70%C_1: (a) flow field and (b) pressure distribution on the plane located at 0.5R from the hub

From Figures 12-16, it is possible to appreciate the detachment of the flow at the trailing edge of the profiles studied. Figures 12-15 allow identifying that this detaching is delayed in multi-element and Gurney flap configurations, which explains the increase of C_L of these profiles. This increase in the C_L improved the torque output of the turbine for the multi-element configurations with and without Gurney flap. Chougule et al. selected a double-element airfoil for the design of a vertical-axis wind turbine. The geometric configuration consisted of a main element and a slat airfoil. It was found that the use of a double-element airfoil instead of a single airfoil increased the C_L and delayed the stall angle [47], as it was achieved in the current research. This fact is highly advantageous for the turbine torque output increase.

Furthermore, as observed in Figures 12, 14 and 16, which were related to the pressure contours, over a cross-section located at 0.5R from the hub of the Geometries A, C and E, the pressure reached minimum values of –3.0385, –3.1507 and –3.6032 kPa in the upper surface of these hydrofoil configurations, respectively. Additionally, maximum values of 14.4186, 15.7175 and 19.6775 kPa in the lower region of the hidrofoil arrangements, respectively, were obtained. As showed in Figures 14-16, the flap had a very important effect on the pressure distributions. In the pressure contours, the multi-element hydrofoil was observed to provide lower pressures than the traditional one, resulting in a minimum negative pressure coefficient higher than in the traditional hydrofoil. Additionally, an increase in the pressure was observed at the stagnation point. In the traditional and in the main element of multi-element hydrofoils, pressure was observed to diminish and increase in the upper and the lower region, respectively, due to the velocity increase. In the multi-element hydrofoil, the flow was trapped beneath the hydrofoil, leading to a decrease in the flow velocities and an increase in the pressure

below the hydrofoil. Therefore, a higher pressure difference is available for the lift generation. In the velocity contours, the fluid was observed to leave the trailing edge of the main element, being deflected and accelerated, and subsequently adhered to the flap. This fact postponed the occurrence of the boundary layer separation, which only occurs in a small area near the trailing edge of the flap. In the traditional hydrofoil, the boundary layer separation was much larger than in the multi-element hydrofoil. The delay in the separation of the boundary layer is one of the factors that contribute to the multi-element hydrofoil, achieving a higher C_L than that observed in the traditional one [18]. Yavuz and coworkers studied the performance of hydrofoil-slat arrangements using NACA 4412 and NACA 6411 hydrofoils. The results showed that the slat also had a significant effect on the pressure distributions [17]. These studies confirm the enhancement of the hydrodynamic performance when the multi-element hydrofoil configuration is employed, as observed in the current study.

The Gurney flap generated a downward turning wake behind the hydrofoil, as observed in Figure 17 in a cross-section of the blade located at 0.5R from the hub. Hence, the hydrofoil effective camber was augmented. In addition, the Gurney flap increased the total pressure on the hydrofoil lower surface. A long wake region downstream the flap was generated, resulting in a delay or elimination of the flow separation at the trailing edge over the upper surface. Such as differences of pressures between the hydrofoil lower and upper surfaces resulted in a circulation rise with an improved lift. In general, the Gurney flap rose both the C_L and C_D of the hydrofoil, being the increase in the C_L value considerably larger, which lead to a high C_{Lmax}/C_D. Therfore, the performance of the hydrofoil was improved [48-50].

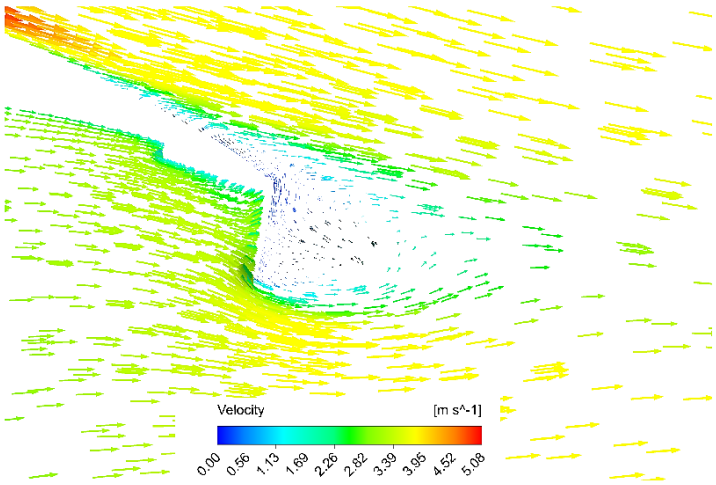

Figure 17. Flow field produced by the Gurney flap

The flap in multi-element configurations provoked a circulation effect on the main element, as represented in Figure 18 in a cross-section of the blade located at 0.5R from the hub. Such as circulation effect resulted in an increase of the lift on the main element. However, the pressure was also increased in that region. The large flow on the trailing element upper surface enabled the flow to leave the main element at a higher velocity, resulting in the main element pressure reduction.

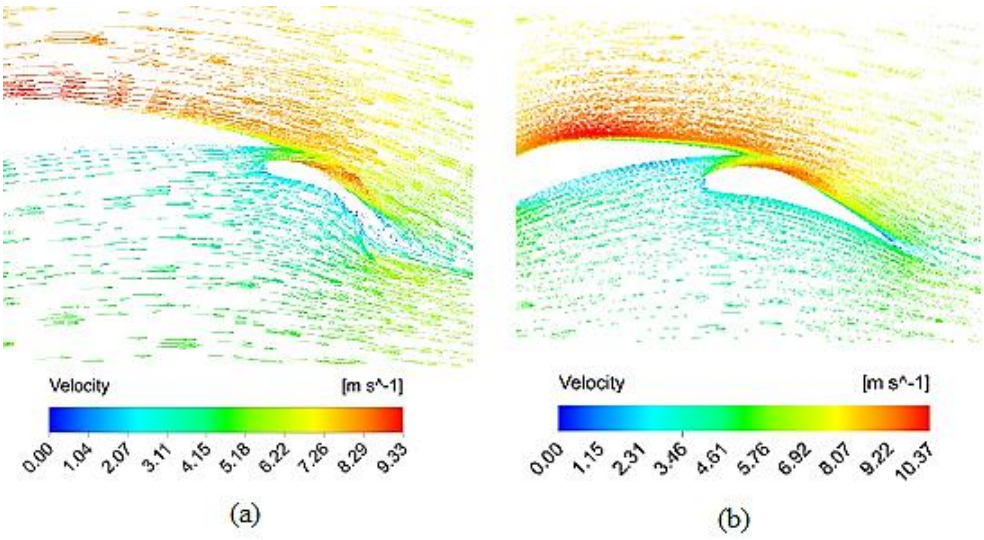

Figure 18. Flow field produced by the main element: (a) geometry D and (b) geometry E on plane at 0.5R blade length

The operating principle of the multi-element profile has been reported in detail by Smith [13] and validated by several researches, which informed that the purpose of a multi-element profile is to increase the C_L without separating the flow and delaying the stall angle in comparison with a traditional configuration [17, 47, 51]. This fact was validated with the geometric configurations studied in the current work, since a C_L rise was observed using multi-element hydrofoils with and without Gurney flap arrangements. This is very useful for the hydrokinetic turbine performance, as the amount of power captured is increased with the subsequent low cost in energy transformation.

Structural Analysis Results

The stresses and displacements were calculated for the same geometries used in CFD analysis using different materials, under hydrodynamic, centrifugal, and gravitational loads. In Figure 19, the results obtained for maximum von Mises stresses and displacements over the blade entire geometry are illustrated. As it is worldwide known, the von Mises stress is a value used to determine when a given material will yield or fracture. The von Mises yield criterion states that if the von Mises stress of a material under load is equal or greater than the yield limit of the same material under a simple tension, then the material will yield [53]. Therefore, according to the von Mises criterion, failure occurres when the value on the left side represented by Eq. (11) reaches the value represented on the right side, where σ_I, σ_{II}, and σ_{III} are the principal stresses action on the blade, and σ_Y refers to the yield stress [52].

$$(\sigma_I - \sigma_{II})^2 + (\sigma_I - \sigma_{III})^2 + (\sigma_{II} - \sigma_{III})^2 = 2\sigma_Y^2 \tag{11}$$

With regard to the material mechanical strength for yielding purposes, the established limit values for the stresses were not surpassed in any blade region. For all the geometries tested, the stresses were maximum at the root of the blade, as represented by Figure 19, where the maximum stress and its location over the geometry E are illustrated. The large C near the blade root is favorable for resisting the large bending moments experienced by the blade when it is operated, while the smaller chord close to the blade tip results in a thinner hydrofoil profile, leading to a drag reduction and a hydrodynamic performance improvement. The geometries C, D and E with a multi-element blade made of steel AISI 304 showed higher levels of stress than the other models. Only, the stresses exhibited in some regions of the blade of geometry D made of steel AISI 304 achieved the mechanical strength limit values of the material for yielding.

Under load, an excessive blade deformation may influence the turbine output power, rising the likelihood of failure. The blades with a multi-element hydrofoil (geometry C and D), which were made of aluminum, reached a maximum displacement of 8.09 and 8.00 mm, respectively, at the tip vs. 1.33 mm of displacement of the blade with only a main hydrofoil (geometry A) made of steel AISI 304. It is noteworthy that the turbine output power can be affected by such as deformations, since the effective α is changing. Therefore, increasing the blade section thickness and reducing the displacement of the blade tip for these geometries are crucial aspects for analyzing their effect on the performance of the blade.

It is important to note that the structural analysis showed high loads in the flap. In this regard, a larger flap is needed to increase its thickness and strength. This fact was demonstrated in the current study when the chord length of the flap changed from 30%C_1 (C geometry) to 70%C_1 (geometry E).

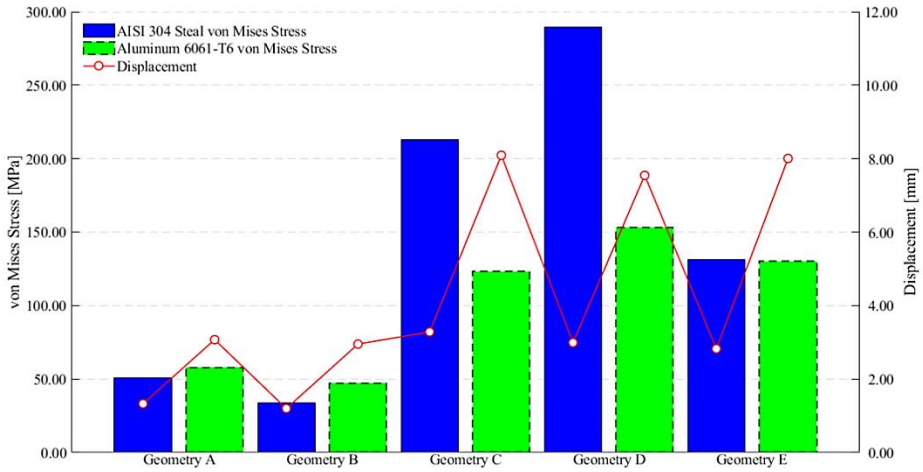

Figure 19. Maximum von Mises stress and displacement values over the blade geometries studied

CONCLUSIONS

The numerical analyses obtained by using JavaFoil code informed that the hydrofoils with multi-element configurations had a C_L higher than the traditional profiles with and without a Gurney flap. This fact can be attributed to the contact surface increase by the flap, which results in a decrease in the flow separation along the blades. The Eppler 420 multi-element configurations with flap lengths of 30% and 70%C_1 resulted to have C_{Lmax} and C_{Lmax}/C_D values equal to 3.69 and 47.77, and 3.87 and 56.29, respectively. In turn, a C_L and a C_{Lmax}/C_D equal to 2.57 and 24.47, respectively, was achieved for the Eppler 420 traditional profile. Additionally, the Eppler 420 traditional profile with a Gurney flap of 4%C length had a C_L equal to 2.82 and a C_{Lmax}/C_D equal to 19.20. The Eppler 420 multi-element configuration with a Gurney flap resulted to have a C_L of 3.85 and a C_{Lmax}/C_D of 39.48 when the Gurney flap size was 3.5%C. Therefore, the Gurney flap led to a C_L rise in comparison with a traditional hydrofoil. Nevertheless, a high Gurney flap might lead to a rise in C_L and C_D simultaneously. Gurney flap sizes lower than 4.0%C might lead to an increased in C_L in the order of 8.8%, with only a slight increase in C_D. Therefore, Gurney flaps are simple mechanical devices with a significant impact on the hydrodynamic performance of hydrofoils.

For the Eppler 420 multi-element hydrofoil, C_{Lmax}/C_D increased with the flap length rise up to 70%C_1. Beyond this value, the benefits ascribed to the multi-element profile are decreased. Each hydrofoil with a multi-element configuration was characterized by a boundary layer generated on the element referred above. A thick turbulent boundary layer might withstand weaker gradients of pressure in comparison with a thin one. Furthermore, a thick turbulent boundary layer resulted to be more prone to be separated. The thickness of the obtained boundary layer is much higher compared to an ordinary boundary layer. Thus, the optimization of h and d parameters is required to define the best flap location.

ACKNOWLEDGMENTS

The authors gratefully acknowledge the financial support provided by the Colombia Scientific Program within the framework of the call Ecosistema Científico (Contract No. FP44842- 218-2018).

REFERENCES

[1] M. Anyi and B. Kirke, "Evaluation of small axial flow hydrokinetic turbines for remote communities," *Energy for Sustainable Development*, vol. 14, no. 2, pp. 110-116, 2010.

[2] D. Kumar and S. Sarkar, "A review on the technology, performance, design optimization, reliability, techno-economics and environmental impacts of hydrokinetic energy conversion systems," *Renewable and Sustainable Energy Reviews*, vol. 58, pp. 796-813, 2016.

[3] D. Ramirez, A. Rubio-Clemente, and E. Chica, "Design and numerical analysis of an efficient H-Darrieus vertical-axis hydrokinetic turbine," *Journal of Mechanical Engineering and Sciences*, vol. 13, no. 4, pp. 6036-6058, 2019.

[4] K. Kusakana and H. J. Vermaak, "Hydrokinetic power generation for rural electricity supply: Case of South Africa," *Renewable Energy*, vol. 55, pp. 467-473, 2013.

[5] E. Chica and A. Rubio-Clemente, *Design of zero head turbines for power generation*. IntechOpen, 2017.

[6] M. Güney and K. Kaygusuz, "Hydrokinetic energy conversion systems: A technology status review," *Renewable and Sustainable Energy Reviews*, vol. 14, no. 9, pp. 2996-3004, 2010.

[7] M. Khan, G. Bhuyan, M. Iqbal, and J. Quaicoe, "Hydrokinetic energy conversion systems and assessment of horizontal and vertical axis turbines for river and tidal applications: A technology status review," *Applied Energy*, vol. 86, no. 10, pp. 1823-1835, 2009.

[8] H. J. Vermaak, K. Kusakana, and S. P. Koko, "Status of micro-hydrokinetic river technology in rural applications: A review of literature," *Renewable and Sustainable Energy Reviews*, vol. 29, pp. 625-633, 2014.

[9] E. Septyaningrum *et al.*, "Performance analysis of multi-row vertical axis hydrokinetic turbine–straight blade cascaded (VAHT-SBC) turbines array," *Journal of Mechanical Engineering and Sciences*, vol. 13, no. 3, pp. 5665-5688, 2019.

[10] J. F. Manwell, J. G. McGowan, and A. L. Rogers, *Wind Energy Explained: Theory, Design and Application*. John Wiley & Sons, 2010.

[11] S. L. Dixon and C. Hall, *Fluid mechanics and thermodynamics of turbomachinery*. Butterworth-Heinemann, 2013.

[12] A. Ragheb and M. Selig, "Multi-element airfoil configurations for wind turbines," in *29th AIAA Applied Aerodynamics Conference*, 2011, p. 3971.

[13] A. M. Smith, "High-lift aerodynamics," *Journal of Aircraft*, vol. 12, no. 6, pp. 501-530, 1975.

[14] T. Cebeci, E. Besnard, and H. Chen, "Calculation of multielement airfoil flows, including flap wells," in *34th Aerospace Sciences Meeting and Exhibit*, 1996, p. 56.

[15] O. Eisele and G. Pechlivanoglou, "Single and Multi-element Airfoil Performance Simulation Study and Wind Tunnel Validation," in *Wind Energy-Impact of Turbulence*: Springer, 2014, pp. 17-22.

[16] S. Narsipur, B. Pomeroy, and M. Selig, "CFD analysis of multielement airfoils for wind turbines," in *30th AIAA Applied Aerodynamics Conference*, 2012, p. 2781.

[17] T. Yavuz, E. Koç, B. Kılkış, Ö. Erol, C. Balas, and T. Aydemir, "Performance analysis of the airfoil-slat arrangements for hydro and wind turbine applications," *Renewable Energy*, vol. 74, pp. 414-421, 2015.

[18] J. Aguilar, A. Rubio-Clemente, L. Velasquez, and E. Chica, "Design and Optimization of a Multi-Element Hydrofoil for a Horizontal-Axis Hydrokinetic Turbine," *Energies*, vol. 12, no. 24, p. 4679, 2019.

[19] R. H. Liebeck, "Design of subsonic airfoils for high lift," *Journal of Aircraft*, vol. 15, no. 9, pp. 547-561, 1978.

[20] J. Kentfield, "Theoretically and experimentally obtained performances of gurney-flap equipped wind turbines," *Wind Engineering*, pp. 63-74, 1994.

[21] A. Bianchini, F. Balduzzi, D. Di Rosa, and G. Ferrara, "On the use of Gurney Flaps for the aerodynamic performance augmentation of Darrieus wind turbines," *Energy Conversion and Management*, vol. 184, pp. 402-415, 2019.

[22] J. E. Dusek, "Leading edge vortex detection using bio-inspired on-body pressure sensing," Massachusetts Institute of Technology, 2011.

[23] Y. Azargoon, M. H. Djavareshkian, and E. Esmaeilifar, "Effect of airfoil distance to water surface on static stall," *Journal of Mechanical Engineering and Sciences*, vol. 14, no. 1, pp. 6526-6537, 2020.

[24] E. A. Bah, L. Sankar, and J. Jagoda, "Investigation on the Use of Multi-Element Airfoils for Improving Vertical Axis Wind Turbine Performance," in *51st AIAA Aerospace Sciences Meeting Including The New Horizons Forum and Aerospace Exposition*, 2013, p. 1109.

[25] A. M. Ragheb and M. S. Selig, "Multielement Airfoils for Wind Turbines," in *Wind Energy Engineering*: Elsevier, 2017, pp. 203-219.

[26] M. Hepperle, "JAVAFOIL user's guide," *available at: www. mh-aerotools. de/airfoils/java/JavaFoil% 20Users% 20Guide. pdf (accessed 12 October 2015)*, 2011.

[27] A. Muratoglu and M. I. Yuce, "Performance Analysis of Hydrokinetic Turbine Blade Sections," *Journal ISSN*, vol. 2, 2015.

[28] D. H. Neuhart, *A water tunnel study of Gurney flaps*. National Aeronautics and Space Administration, Scientific and Technical …, 1988.

[29] K. M. Andreadis, G. J. P. Schumann, and T. Pavelsky, "A simple global river bankfull width and depth database," *Water Resources Research*, vol. 49, no. 10, pp. 7164-7168, 2013.

[30] B. Kirke, "Hydrokinetic and ultra-low head turbines in rivers: A reality check," *Energy for Sustainable Development*, vol. 52, pp. 1-10, 2019.

[31] M. R. Ahmed, "Blade sections for wind turbine and tidal current turbine applications–current status and future challenges," *International Journal of Energy Research*, vol. 36, no. 7, pp. 829-844, 2012.

[32] J. N. Goundar, M. R. Ahmed, and Y.-H. Lee, "Numerical and experimental studies on hydrofoils for marine current turbines," *Renewable energy*, vol. 42, pp. 173-179, 2012.

[33] E. Chica, F. Perez, A. Rubio-Clemente, and S. Agudelo, "Design of a hydrokinetic turbine," *WIT Trans. Ecol. Environ*, vol. 195, pp. 137-148, 2015.

[34] C. Yorke and G. Coleman, "Assessment of common turbulence models for an idealised adverse pressure gradient flow," *European Journal of Mechanics-B/Fluids*, vol. 23, no. 2, pp. 319-337, 2004.

[35] S. Dajani *et al.*, "Numerical Study for a Marine Current Turbine Blade Performance under Varying Angle of Attack," *Energy Procedia*, vol. 119, pp. 898-909, 2017.

[36] C. Daskiran, J. Riglin, and A. Oztekin, "Computational study of multiple hydrokinetic turbines: the effect of wake," in *ASME International Mechanical Engineering Congress and Exposition*, 2015, vol. 57465: American Society of Mechanical Engineers, p. V07AT09A021.

[37] F. Bassi, L. Botti, A. Colombo, A. Ghidoni, and S. Rebay, "Investigation of near-wall grid spacing effect in high-order discontinuous Galerkin RANS computations of turbomachinery flows," in *Spectral and High Order Methods for Partial Differential Equations-ICOSAHOM 2012*: Springer, 2014, pp. 125-134.

[38] A. Bouhelal, A. Smaili, O. Guerri, and C. Masson, "Numerical investigation of turbulent flow around a recent horizontal axis wind Turbine using low and high Reynolds models," *Journal of Applied Fluid Mechanics*, vol. 11, no. 1, pp. 151-164, 2018.

[39] M. Moshfeghi, Y. J. Song, and Y. H. Xie, "Effects of near-wall grid spacing on SST-K-ω model using NREL Phase VI horizontal axis wind turbine," *Journal of Wind Engineering and Industrial Aerodynamics*, vol. 107, pp. 94-105, 2012.

[40] D. C. Wilcox, "Reassessment of the scale-determining equation for advanced turbulence models," *AIAA journal*, vol. 26, no. 11, pp. 1299-1310, 1988.

[41] H. Schlichting and K. Gersten, *Boundary-layer theory*. Springer, 2016.

[42] M. M. S. Reza, S. A. Mahmood, and A. Iqbal, "Performance Analysis and Comparison of High Lift Airfoil for Low Speed Unmanned Aerial Vehicle," in *International Conference on Mechanical, Industrial and Energy Engineering*, 2016, pp. 26-27.

[43] J. Wang, Y. Li, and K.-S. Choi, "Gurney flap—Lift enhancement, mechanisms and applications," *Progress in Aerospace Sciences*, vol. 44, no. 1, pp. 22-47, 2008.

[44] I. Aramendia, U. Fernandez-Gamiz, E. Zulueta, A. Saenz-Aguirre, and D. Teso-Fz-Betoño, "Parametric study of a gurney flap implementation in a du91w (2) 250 airfoil," *Energies*, vol. 12, no. 2, p. 294, 2019.

[45] S. Jain, N. Sitaram, and S. Krishnaswamy, "Computational investigations on the effects of Gurney flap on airfoil aerodynamics," *International Scholarly Research Notices*, vol. 2015, 2015.

[46] E. C. Arrieta, J. A. Bedoya, and A. R. Clemente, "Investigación numérica sobre el uso de álabes multielemento en turbina hidrocinética de eje horizontal," *Revista UIS Ingenierías*, vol. 18, no. 3, pp. 117-128, 2019.

[47] P. Chougule and S. R. Nielsen, "Simulation of flow over double-element airfoil and wind tunnel test for use in vertical axis wind turbine," in *Journal of Physics: Conference Series*, 2014, vol. 524, no. 1: IOP Publishing, p. 012009.

[48] M. Chandrasekhara, "Optimum Gurney flap height determination for "lost-lift" recovery in compressible dynamic stall control," *Aerospace Science and Technology*, vol. 14, no. 8, pp. 551-556, 2010.

[49] M. D. Maughmer and G. Bramesfeld, "Experimental investigation of Gurney flaps," *Journal of Aircraft*, vol. 45, no. 6, pp. 2062-2067, 2008.

[50] Y. Amini, M. Liravi, and E. Izadpanah, "The effects of Gurney flap on the aerodynamic performance of NACA 0012 airfoil in the rarefied gas flow," *Computers & Fluids*, vol. 170, pp. 93-105, 2018.

[51] W. K. Anderson, D. L. Bonhaus, R. J. McGhee, and B. S. Walker, "Navier-Stokes computations and experimental comparisons for multielement airfoil configurations," *Journal of Aircraft*, vol. 32, no. 6, pp. 1246-1253, 1995.

[52] A. Muñoz, L. Chiang, and E. De la Jara, "A design tool and fabrication guidelines for small low cost horizontal axis hydrokinetic turbines," *Energy for Sustainable Development*, vol. 22, pp. 21-33, 2014.